Nonpotential effects in dynamics of fronts between convection patterns

A. Hari[1] and A. A. Nepomnyashchy[1,2]
[1]*Department of Mathematics, Technion–Israel Institute of Technology, 32000 Haifa, Israel*
[2]*Minerva Center for Physics of Complex Systems, Technion–Israel Institute of Technology, 32000 Haifa, Israel*
(Received 25 June 1999)

The dynamics of fronts between hexagonal convection patterns and a mechanical equilibrium state are investigated in the cases where the hexagons are stable and the equilibrium is either stable or unstable. The Newell-Whitehead-Segel, equations with additional nonpotential terms are used. The velocity of the domain boundary between two competing convection patterns and the wave number selected in the presence of the front are calculated.

PACS number(s): 82.40.Ck, 47.7.Te, 47.54.+r

I. INTRODUCTION

A typical feature of nonlinear pattern-forming systems is multistability, e.g., coexistence of different stable patterns at the same value of the overcriticality parameter ϵ. For instance, hexagonal patterns may coexist with the uniform state, rolls [1], squares [2,3], and quasiperiodic patterns [4]. The multistability leads to formation of *fronts* [5] between different patterns which may move, ousting a ''less favorable'' pattern. Near the onset of pattern formation, analysis of the pattern selection and propagation of fronts may be performed by means of amplitude equations [6,7]. In potential systems, which have a Lyapunov functional decreasing with time, the direction of the front motion is determined by the condition of the Lyapunov functional decrease. The normal velocity of the front depends on the difference between Lyapunov functional densities of the two patterns and on the orientation of the front with respect to the basic wave vectors of the patterns [5,8,9].

Recently, it was realized that the amplitude equations describing hexagonal patterns generally contain some nonpotential terms that do not vanish even near the threshold [10–15]. In the leading order, these equations can be written in the following form:

$$\frac{\partial A_l}{\partial t}=\gamma A_l+\frac{\partial^2 A_l}{\partial x_l^2}-(|A_l|^2+\lambda|A_{[l-1]}|^2+\lambda|A_{[l+1]}|^2)A_l + A^*_{[l-1]}A^*_{[l+1]}+i\hat{K}\left(A^*_{[l+1]}\frac{\partial A^*_{[l-1]}}{\partial y_{[l-1]}}-A^*_{[l-1]}\frac{\partial A^*_{[l+1]}}{\partial y_{[l+1]}}\right) + i\hat{B}\left(A^*_{[l+1]}\frac{\partial A^*_{[l-1]}}{\partial x_{[l-1]}}+A^*_{[l-1]}\frac{\partial A^*_{[l+1]}}{\partial x_{[l+1]}}\right), \quad l=0,1,2, \tag{1}$$

where A_l are complex envelope functions of the ''slow'' time variable t and space variable $\mathbf{r}$ which correspond to basic wave vectors $k_c\mathbf{n}_l$ [6], k_c being the critical wave number in the linear stability theory. $x_l\equiv\mathbf{r}\cdot\mathbf{n}_l$, $y_l\equiv\mathbf{r}\cdot\boldsymbol{\tau}_l$, where $\mathbf{n}_l$ and $\boldsymbol{\tau}_l$ are pairs of mutually orthogonal unit vectors (the rotation from $\mathbf{n}_l$ to $\boldsymbol{\tau}_l$ is counterclockwise), $\mathbf{n}_0+\mathbf{n}_1+\mathbf{n}_2=\mathbf{0}$, and $[l\pm1]\equiv(l\pm1)$ (mod3).

In convection problems, the coefficient $\hat{K}$ is generally nonzero if the boundary conditions on the upper and lower boundaries of the fluid layer are not identical [13]. The term with $\hat{B}$ has been derived in the case of Marangoni convection [14,15] and non-Boussinesq Rayleigh-Bénard convection [10]. The appearance of nonpotential terms containing $\hat{K}$ and $\hat{B}$ in equations for envelope functions is caused by the fact that the nonlinear coefficient describing the resonant interaction of three Fourier modes [16] is not a constant but depends on the wave vectors of these modes. The nonpotential terms produce some effects violating the well-known similarity between the nonequilibrium pattern formation and equilibrium phase transitions [5].

Because the nonpotential terms contain spatial derivatives of amplitudes, they do not appear in the case where the amplitudes do not depend on spatial coordinates (which corresponds to perfect patterns with all wave numbers equal to k_c); thus a Lyapunov functional can be constructed and calculated for different kinds of *perfect* patterns. However, in contradistinction to the potential case studied by Pomeau [5], the comparison of densities of the Lyapunov functional for different uniform patterns provides generally no information about the direction of the motion of the fronts between them, because the nonuniform system, which contains a front, has no functional that tends to decrease.

Another peculiarity of the pattern formation governed by the nonpotential system of equations (1) is a nontrivial *wave number selection* in the presence of a front. In the case of the standard Newell-Whitehead-Segel equations, the critical wave number k_c providing the minimal value of the Lyapunov functional is usually selected [8]. In the nonpotential case, there are no reasons for such a choice.

When the parameters of the system are changed, some of the competing patterns may become unstable, and instead of a front between two locally stable structures, one obtains a front between a stable state and an unstable state. The propagation of a stable hexagonal pattern ousting an unstable quiescent state and unstable roll patterns was formerly investigated in [17] in the framework of a potential model ($\hat{K}=\hat{B}=0$). Both ''generic'' and ''nongeneric'' fronts (see [18,19]) were found. Recently, Csahók and Misbah [20] studied the same problem in the framework of a nonpotential model connected with the damped Kuramoto-Sivashinsky

equation, by means of direct numerical simulations of the latter equation. The most remarkable phenomenon observed in these simulations was splitting of the front into two fronts moving with the same velocity.

In the present paper, a systematic investigation of the influence of nonpotential effects on the propagation of a hexagonal pattern into the quiescent state is given. In Sec. II, we consider the dynamics of a front between a stable hexagonal pattern and a stable quiescent state. We discuss the nontrivial wave number selection for the hexagonal patterns and the change of the front velocity due to the nonpotential terms. Section III is devoted to investigation of different kinds of fronts between stable hexagons and an unstable quiescent state. We analyze the appearance of the roll strip and the nonuniqueness of front solutions, and suggest a criterion for the selection of the roll strip length. We suggest also an explanation of the synchronization of velocities of the roll strip boundaries. Section IV contains some concluding remarks.

II. FRONTS BETWEEN STABLE PATTERNS

In this section we study the competition between the stable hexagonal pattern and the stable quiescent state that coexist on an infinite plane $-\infty<x<\infty$, $-\infty<y<\infty$. The basic wave vectors of the hexagonal patterns are chosen as follows:

$$\mathbf{n}_0=(1,0), \quad \mathbf{n}_1=\left(-\frac{1}{2},\frac{\sqrt{3}}{2}\right), \quad \mathbf{n}_2=\left(-\frac{1}{2},-\frac{\sqrt{3}}{2}\right). \tag{2}$$

A. Potential case

First, let us recall the main facts concerning the fronts in the potential case [5,8]. Consider a front that is plane and parallel to the axis y, so that we can assume that the amplitudes A_l, $l=0$, 1, 2, do not depend on y. Recall that in the absence of nonpotential terms ($\hat{K}=\hat{B}=0$), the system of amplitude equations can be written in the form

$$\frac{\partial A_l}{\partial t}=-\frac{\delta\mathcal{L}}{\delta A_l^*}, \quad l=0,1,2, \tag{3}$$

where the Lyapunov functional is

$$\mathcal{L}=\int_{-\infty}^{\infty}L(x,t)dx, \tag{4}$$

$$L=\sum_{l=0}^{2}\frac{1}{2}\left|\frac{\partial A_l}{\partial x}\right|^2 n_{lx}^2-V, \tag{5}$$

and the potential

$$V=\sum_{l=0}^{2}\left(\tfrac{1}{2}\gamma|A_l|^2-\tfrac{1}{4}|A_l|^4\right)-\frac{\lambda}{2}\left(|A_0|^2|A_1|^2+|A_1|^2|A_2|^2+|A_2|^2|A_0|^2\right)+A_1^*A_2^*A_0^*. \tag{6}$$

The equations for A_1 and A_2 are fully symmetric; thus there exists the invariant manifold $A_2=A_1$. Disregarding phase disturbances, we can assume that A_l are real. Finally, denoting $A_0=A$, $A_1=A_2=B$, we obtain the following system of equations:

$$\begin{aligned}\frac{\partial A}{\partial t}&=\frac{\partial^2 A}{\partial x^2}+\gamma A+B^2-A^3-2\lambda AB^2,\\ \frac{\partial B}{\partial t}&=\frac{1}{4}\frac{\partial^2 B}{\partial x^2}+\gamma B+AB-(1+\lambda)B^3-\lambda A^2B.\end{aligned} \tag{7}$$

Both hexagonal patterns, which are described by the solution

$$A=B\equiv A_h=\frac{1+\sqrt{1+4\gamma(1+2\lambda)}}{2(1+2\lambda)}, \tag{8}$$

and the quiescent state (mechanical equilibrium)

$$A=B=0 \tag{9}$$

are linearly stable in the region

$$-\frac{1}{4(1+2\lambda)}<\gamma<0. \tag{10}$$

Note that the solution $A=A_h$, $B=-A_h$ corresponds to a spatially shifted hexagonal pattern, and it is unnecessary to separately consider the front between that pattern and the quiescent state.

A front between the hexagonal pattern (8) and the quiescent state (9), which moves with the constant velocity c,

$$A(x,t)=\overline{A}(\xi), \quad B(x,t)=\overline{B}(\xi), \quad \xi=x-ct, \tag{11}$$

is governed by the following system of equations:

$$\frac{d^2\overline{A}}{d\xi^2}+c\frac{d\overline{A}}{d\xi}+\gamma\overline{A}+\overline{B^2}-\overline{A^3}-2\lambda\overline{B^2}\overline{A}=0, \tag{12}$$

$$\frac{1}{4}\frac{d^2\overline{B}}{d\xi^2}+c\frac{d\overline{B}}{d\xi}+\gamma\overline{B}+\overline{AB}-(1+\lambda)\overline{B^3}-\lambda\overline{A^2}\overline{B}=0, \tag{13}$$

with boundary conditions

$$\begin{aligned}\overline{A}=\overline{B}=A_h \quad &\text{as} \quad \xi\to-\infty,\\ \overline{A}=\overline{B}=0 \quad &\text{as} \quad \xi\to\infty.\end{aligned} \tag{14}$$

Both stationary points $\overline{A}=\overline{B}=A_h$ and $\overline{A}=\overline{B}=0$ correspond to maxima of the potential,

$$V(\overline{A},\overline{B})=\tfrac{1}{2}\gamma(\overline{A^2}+2\overline{B^2})+\overline{AB^2}-\left[\tfrac{1}{4}\overline{A^4}+\lambda\overline{A^2}\overline{B^2}+\tfrac{1}{2}(1+\lambda)\overline{B^4}\right]. \tag{15}$$

For any γ satisfying the conditions (10), there exists a unique value $c(\gamma)$ such that the problem (12), (13) with the boundary conditions (14) has a solution. The typical dependence $c(\gamma)$ is shown in Fig. 1 (recall that we consider now only the region $\gamma<0$). The front is motionless ($c=0$) as

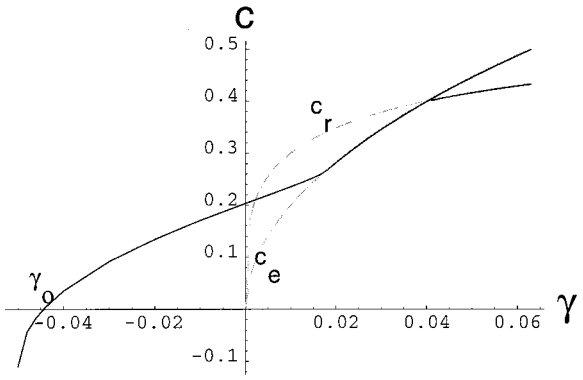

FIG. 1. The velocity of the hexagon-equilibrium front c vs γ in the potential case. The light lines correspond to the velocities c_e and c_r given by the marginal stability criterion. The dark lines correspond to the velocities calculated from our numerical results. On the right, where the dark line is split, these are the velocities of the two separate fronts in region C; the upper is c_e and the lower is c_r. These measured velocities coincide with the calculated ones. All calculations were made for $\lambda=2$.

$$\gamma=\gamma_0=-\frac{2}{9(1+2\lambda)}. \tag{16}$$

B. Nonpotential case

It is convenient to rewrite the system (1) in the form [14]

$$\begin{aligned}\frac{\partial A_n}{\partial t}&=\gamma A_n+(\mathbf{n}_n\cdot\boldsymbol{\nabla})^2A_n+A_l^*A_m^*\\&+i\sum_{m,l\neq n}[A_l^*(a\mathbf{n}_l+b\mathbf{n}_m)\cdot\boldsymbol{\nabla}A_m^*]-|A_n|^2A_n\\&-\lambda(|A_l|^2+|A_m|^2)A_n,\quad n=0,1,2,\ l,m\neq n,\end{aligned} \tag{17}$$

where

$$a=-\frac{2}{\sqrt{3}}\hat{K}\quad\text{and}\quad b=\hat{B}-\frac{1}{\sqrt{3}}\hat{K}.$$

1. Wave number selection near the point $\gamma=\gamma_0$

In the case of a stable-stable front, the nonpotential terms lead to two main effects: (1) nontrivial wave number selection of the hexagonal pattern; and (2) change of the front velocity. In order to elucidate the origin of those effects, let us analyze in more detail the influence of *weak* nonpotential terms on the behavior of the front near the point $\gamma=\gamma_0$ defined by Eq. (16). We allow some deviation of the wave vectors around the wave vectors given by Eq. (2); thus we assume

$$\begin{aligned}A_0&=\hat{A}(x,t)\exp(ik_0x),\\A_1&=\hat{B}(x,t)\exp[-ik_0(\tfrac{1}{2}x-\varphi y)],\\A_2&=\hat{B}(x,t)\exp[-ik_0(\tfrac{1}{2}x+\varphi y)].\end{aligned} \tag{18}$$

Substituting Eq. (18) into Eq. (1), we find

$$\begin{aligned}\frac{\partial\hat{A}}{\partial t}&=(\gamma-k_0^2)\hat{A}+\frac{\partial^2\hat{A}}{\partial x^2}+2ik_0\frac{\partial\hat{A}}{\partial x}\\&+\left(1+\frac{k_0}{2}(a+b)-\sqrt{3}\varphi k_0(a-b)\right)(\hat{B}^*)^2\\&-i(a+b)\frac{\partial\hat{B}^*}{\partial x}\hat{B}^*-|\hat{A}|^2\hat{A}-2\lambda|\hat{B}|^2\hat{A},\end{aligned} \tag{19}$$

$$\begin{aligned}\frac{\partial\hat{B}}{\partial t}&=\left[\gamma-k_0^2\left(\frac{1}{4}+\frac{\sqrt{3}}{2}\varphi\right)^2\right]\hat{B}+\frac{1}{4}\frac{\partial^2\hat{B}}{\partial x^2}-ik_0\left(\frac{1}{4}+\frac{\sqrt{3}}{2}\varphi\right)\frac{\partial\hat{B}}{\partial x}\\&+\left(1-k_0(a-\tfrac{5}{4}b)-\frac{\sqrt{3}}{2}\varphi k_0b\right)\hat{A}^*\hat{B}^*\\&+i(a-\tfrac{1}{2}b)\frac{\partial\hat{B}^*}{\partial x}\hat{A}^*+i(b-\tfrac{1}{2}a)\frac{\partial\hat{A}^*}{\partial x}\hat{B}^*\\&-(1+\lambda)|\hat{B}|^2\hat{B}-\lambda|\hat{A}|^2\hat{B}.\end{aligned} \tag{20}$$

We will investigate a front moving with velocity c; therefore we assume

$$\begin{aligned}\hat{A}(x,t)&=\overline{A}(\xi),\\\hat{B}(x,t)&=\overline{B}(\xi),\end{aligned} \tag{21}$$

where $\xi=x-ct$. Note that the amplitudes $A_j(x,t)$, $j=0,1,2$, are not functions of ξ only, because the hexagonal pattern itself does not move. Substituting Eq. (21) into Eqs. (19) and (20), one finds

$$\begin{aligned}&\frac{d^2\overline{A}}{d\xi^2}+(2ik_0+c)\frac{d\overline{A}}{d\xi}+(\gamma-k_0^2)\overline{A}\\&+\left(1+\frac{k_0}{2}(a+b)-\sqrt{3}\varphi k_0(a-b)\right)(\overline{B}^*)^2\\&-i(a+b)\frac{d\overline{B}^*}{d\xi}\overline{B}^*-|\overline{A}|^2\overline{A}-2\lambda|\overline{B}|^2\overline{A}=0,\end{aligned} \tag{22}$$

$$\begin{aligned}&\frac{1}{4}\frac{d^2\overline{B}}{d\xi^2}+\left[c-ik_0\left(\frac{1}{4}+\frac{\sqrt{3}}{2}\varphi\right)\right]\frac{d\overline{B}}{d\xi}+\left[\gamma-k_0^2\left(\frac{1}{4}+\frac{\sqrt{3}}{2}\varphi\right)^2\right]\overline{B}\\&+\left(1-k_0(a-\tfrac{5}{4}b)-\frac{\sqrt{3}}{2}\varphi k_0b\right)\overline{A}^*\overline{B}^*\\&+i(a-\tfrac{1}{2}b)\frac{d\overline{B}^*}{d\xi}\overline{A}^*+i(b-\tfrac{1}{2}a)\frac{d\overline{A}^*}{d\xi}\overline{B}^*\\&-(1+\lambda)|\overline{B}|^2\overline{B}-\lambda|\overline{A}|^2\overline{B}=0.\end{aligned} \tag{23}$$

Assume that a, b, and k_0 are very small, of the order of magnitude of ϵ, $0<\epsilon\ll1$, and substitute $\gamma=\gamma_0=-2/[9(1+2\lambda)]$, $a=\epsilon\overline{a}$, $b=\epsilon\overline{b}$, $k_0=\epsilon\overline{k_0}$, $c=\epsilon c_1+\epsilon^2c_2+o(\epsilon^2)$, $\overline{A}$

$=\overline{A}_0+\epsilon\overline{A}_1+o(\epsilon)$, and $\overline{B}=\overline{B}_0+\epsilon\overline{B}_1+o(\epsilon)$ into Eqs. (22) and (23) ($\overline{A}_0$ and $\overline{B}_0$ can be chosen real).

In the leading order $O(1)$, we obtain the equations

$$\gamma_0\overline{A}_0+\frac{d^2\overline{A}_0}{d\xi^2}+\overline{B}_0^2-\overline{A}_0^3-2\lambda\overline{B}_0^2\overline{A}_0=0, \tag{24}$$

$$\gamma_0\overline{B}_0+\frac{1}{4}\frac{d^2\overline{B}_0}{d\xi^2}+\overline{A}_0\overline{B}_0-(1+\lambda)\overline{B}_0^3-\lambda\overline{A}_0^2\overline{B}_0=0, \tag{25}$$

which coincide with those for the potential problem.

In the order $O(\epsilon)$ we find

$$\begin{aligned}&\gamma_0\overline{A}_1+\frac{d^2\overline{A}_1}{d\xi^2}+2\overline{B}_0\overline{B}_1^*-2\overline{A}_0^2\overline{A}_1-\overline{A}_0^2\overline{A}_1^*\\&\quad-2\lambda(\overline{A}_0\overline{B}_0\overline{B}_1+\overline{A}_0\overline{B}_0\overline{B}_1^*+\overline{B}_0^2\overline{A}_1)\\&\quad=-(2i\overline{k}_0+c_1)\frac{d\overline{A}_0}{d\xi}+i(\overline{a}+\overline{b})\frac{d\overline{B}_0}{d\xi}\overline{B}_0,\end{aligned} \tag{26}$$

$$\begin{aligned}&\gamma_0\overline{B}_1+\frac{1}{4}\frac{d^2\overline{B}_1}{d\xi^2}+\overline{A}_0\overline{B}_1^*+\overline{B}_0\overline{A}_1^*-(1+\lambda)(2\overline{B}_0^2\overline{B}_1+\overline{B}_0^2\overline{B}_1^*)\\&\quad-\lambda(\overline{A}_0\overline{B}_0\overline{A}_1+\overline{A}_0\overline{B}_0\overline{A}_1^*+\overline{A}_0^2\overline{B}_1)\\&\quad=-\left[c_1-i\overline{k}_0\left(\frac{1}{4}+\frac{\sqrt{3}}{2}\varphi\right)\right]\frac{dB_0}{d\xi}-i(\overline{a}-\tfrac{1}{2}\overline{b})\\&\quad\times\overline{A}_0\frac{d\overline{B}_0}{d\xi}-i(\overline{b}-\tfrac{1}{2}\overline{a})\overline{B}_0\frac{d\overline{A}_0}{d\xi}.\end{aligned} \tag{27}$$

Separating real and imaginary parts of $\overline{A}_1$ and $\overline{B}_1$:

$$\begin{aligned}\overline{A}_1&=\overline{A}_{1,r}+i\overline{A}_{1,i},\\\overline{B}_1&=\overline{B}_{1,r}+i\overline{B}_{1,i},\end{aligned} \tag{28}$$

and multiplying by 2 both sides of Eq. (27), we obtain two inhomogeneous linear problems, one for the real parts,

$$\begin{aligned}&\left(\frac{d^2}{d\xi^2}+\gamma_0-3\overline{A}_0^2-2\lambda\overline{B}_0^2\right)\overline{A}_{1,r}+(2\overline{B}_0-4\lambda\overline{A}_0\overline{B}_0)\overline{B}_{1,r}\\&\quad=-c_1\frac{d\overline{A}_0}{d\xi},\end{aligned} \tag{29}$$

$$\begin{aligned}&(2\overline{B}_0-4\lambda\overline{A}_0\overline{B}_0)\overline{A}_{1,r}+\left(\frac{1}{2}\frac{d^2}{d\xi^2}+2\gamma_0+2\overline{A}_0\right.\\&\left.\quad-2\lambda\overline{A}_0^2-6(1+\lambda)\overline{B}_0^2\right)\overline{B}_{1,r}=-2c_1\frac{d\overline{B}_0}{d\xi},\end{aligned} \tag{30}$$

and another one for the imaginary parts of the functions,

$$\begin{aligned}&\left(\frac{d^2}{d\xi^2}+\gamma_0-\overline{A}_0^2-2\lambda\overline{B}_0^2\right)\overline{A}_{1,i}-2\overline{B}_0\overline{B}_{1,i}\\&\quad=-2\overline{k}_0\frac{\partial\overline{A}_0}{\partial\xi}+(\overline{a}+\overline{b})\frac{\partial\overline{B}_0}{\partial\xi}\overline{B}_0,\end{aligned} \tag{31}$$

$$\begin{aligned}&-2\overline{B}_0\overline{A}_{1,i}+\left(\frac{1}{2}\frac{d^2}{d\xi^2}+2\gamma_0-2\overline{A}_0-2\lambda\overline{A}_0^2-2(1+\lambda)\overline{B}_0^2\right)\overline{B}_{1,i}\\&\quad=\overline{k}_0(\tfrac{1}{2}+\sqrt{3}\varphi)\frac{d\overline{B}_0}{d\xi}-(2\overline{a}-\overline{b})\overline{A}_0\frac{d\overline{B}_0}{d\xi}\\&\quad-(2\overline{b}-\overline{a})\overline{B}_0\frac{d\overline{A}_0}{d\xi}.\end{aligned} \tag{32}$$

The solution of the homogeneous part of the linear equation system (29) and (30) is

$$\begin{aligned}\overline{A}_{1,r}^h&=\frac{d\overline{A}_0}{d\xi},\\\overline{B}_{1,r}^h&=\frac{d\overline{B}_0}{d\xi}.\end{aligned} \tag{33}$$

Since the corresponding linear operator is self-adjoint, the solvability condition is

$$c_1\int_{-\infty}^{\infty}\left[\left(\frac{d\overline{A}_0}{d\xi}\right)^2+2\left(\frac{d\overline{B}_0}{d\xi}\right)^2\right]d\xi=0, \tag{34}$$

which yields the relation

$$c_1=0. \tag{35}$$

The solution of the homogeneous part of the linear system of equations (31) and (32) is

$$\begin{aligned}\overline{A}_{1,i}^h&=\overline{A}_0,\\\overline{B}_{1,i}^h&=-\tfrac{1}{2}\overline{B}_0,\end{aligned} \tag{36}$$

and thus the solvability condition is

$$\begin{aligned}&\int_{-\infty}^{\infty}\overline{A}_0\left(-2\overline{k}_0\frac{d\overline{A}_0}{d\xi}+(\overline{a}+\overline{b})\frac{d\overline{B}_0}{d\xi}B_0\right)d\xi\\&\quad+\int_{-\infty}^{\infty}\left(-\frac{\overline{B}_0}{2}\right)\left((\tfrac{1}{2}+\sqrt{3}\varphi)\overline{k}_0\frac{d\overline{B}_0}{\partial\xi}-(2\overline{a}-\overline{b})\overline{A}_0\frac{d\overline{B}_0}{d\xi}\right.\\&\quad\left.-(2\overline{b}-\overline{a})\overline{B}_0\frac{d\overline{A}_0}{d\xi}\right)d\xi=0,\end{aligned} \tag{37}$$

from which, after multiplying by ϵ, follows the expression for k_0:

$$\begin{aligned}k_0(\varphi)=&\frac{(b-\frac{1}{2}a)A_h^3-3(a-\frac{1}{2}b)\int_{-\infty}^{\infty}\overline{A}_0\overline{B}_0(d\overline{B}_0/d\xi)d\xi}{[\frac{9}{8}+(\sqrt{3}/4)\varphi]A_h^2}\\&+O(\epsilon^2).\end{aligned} \tag{38}$$

Thus we found that there exists a one-parametric family $k_0(\varphi)$ of hexagonlike patterns selected by the coexistence of those patterns with the quiescent state for every φ. In the case $\varphi=\sqrt{3}/2$, we obtain the usual hexagons with shifted wave number; the case $\varphi\neq\sqrt{3}/2$ corresponds to ''nonequilateral'' hexagons [21].

Evaluation of the expression (38), e.g., for $\lambda=2$, $a=b=-0.001$, $\varphi=0$, yields $k_0=-1.182\times10^{-4}$, where the approximated value of $\int_{-\infty}^{\infty}A_0B_0(dB_0/d\xi)d\xi$ is -7.86×10^{-4}. The corresponding hexagons are slightly deformed and are a little ''bigger'' than in the pure potential case.

Note that the change of the front velocity caused by small nonpotential terms is $O(\epsilon^2)$. The expression for c_2 can be obtained from the solvability condition of the equations for $\overline{A}_{2,r}$ and $\overline{B}_{2,r}$ in the next order in ϵ.

2. Numerical simulation of the front motion

We have performed numerical simulations under the assumption

$$A_1=A,\qquad A_2=A_3=B, \tag{39}$$

with the choice (2) of basic wave vectors. In that case, we obtain the following equations:

$$\frac{\partial A}{\partial t}=\gamma A+\frac{\partial^2 A}{\partial x^2}+(B^*)^2-i(a+b)\frac{\partial B^*}{\partial x}B^*-|A|^2A-2\lambda|B|^2A, \tag{40}$$

$$\frac{\partial B}{\partial t}=\gamma B+\frac{1}{4}\frac{\partial^2 B}{\partial x^2}+A^*B^*+i\left(a-\frac{b}{2}\right)\frac{\partial B^*}{\partial x}A^*+i\left(b-\frac{a}{2}\right)\frac{\partial A^*}{\partial x}B^*-(1+\lambda)|B|^2B-\lambda|A|^2B. \tag{41}$$

According to results of the analysis presented above, the solution of Eqs. (40) and (41) does *not* have the form $A=A(x-ct)$, $B=B(x-ct)$, because the hexagonal pattern with $k_0\neq0$, which is formed behind the moving front, is stationary and does not move with the velocity c. Our numerical simulations show, however, that the propagation of the moduli of the amplitudes $|A|$, $|B|$ occurs with a certain constant velocity.

Zero velocity, small a and b. We solved the problem Eqs. (40) and (41) numerically for small a and b ($a=b=-0.001$), and $\gamma=-2/[9(1+2\lambda)]$ such that $v_0\approx0$, with boundary conditions

$$\frac{\partial A_r}{\partial x}=\frac{\partial A_i}{\partial x}=\frac{\partial B_r}{\partial x}=\frac{\partial B_i}{\partial x}=0,\quad \text{as } x=0 \text{ and } x=L=600. \tag{42}$$

For simulations, we used a finite-difference numerical scheme. The results for the absolute values of the amplitudes $|A|$ and $|B|$ and the phases $\Phi_A=\arg A$ and $\Phi_B=\arg B$ are shown in Fig. 2. In the central part of the region, a nonzero value of wave numbers equal to -1.025×10^{-4} is generated, which is close to the value calculated analytically. Because of Eq. (42), the wave numbers $\partial\Phi_A/\partial x$ and $\partial\Phi_B/\partial x$ tend to zero as $x\to0$.

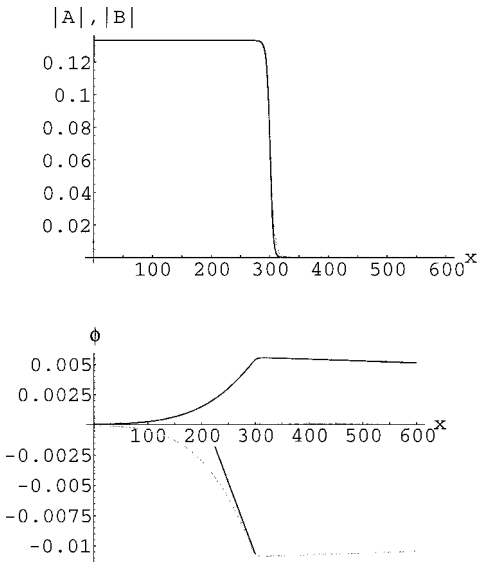

FIG. 2. The envelope shape: the absolute values $|A|$ and $|B|$ and the phases ϕ_A and ϕ_B of the amplitude functions of the convection patterns obtained by numerical simulations of the nonpotential system, with a and b small ($a=b=-0.001$), γ at the value of zero velocity, $\gamma=-2/[9(1+2\lambda)]$, $\lambda=2$. The light lines are for the functions $|A|$ and ϕ_A, and the dark lines are for the functions $|B|$ and ϕ_B. The straight line shown tangential to ϕ_A is the analytically predicted value of the slope calculated in the text.

Nonzero velocity, finite a and b. We solved the system (40) and (41) numerically, with $-1/[4(1+2\lambda)]<\gamma<0$, $\lambda=2$, where both the hexagons and the quiescent state are stable, and $a=b=-1.0$. We calculated the velocity of the propagation of $|A|$, $|B|$ and found that it is slightly different from the velocity obtained in the potential case. The comparison of results obtained for potential and nonpotential systems can be seen in the left side of Fig. 3 ($\gamma<0$).

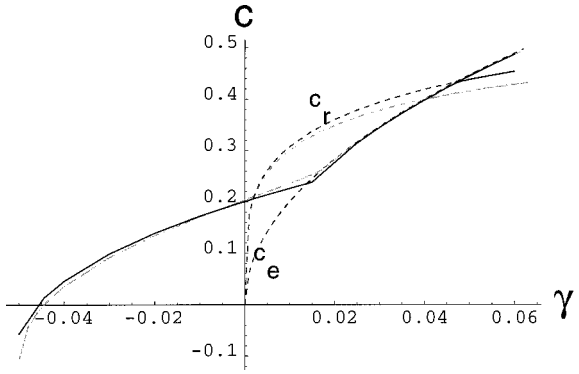

FIG. 3. The front velocity in the nonpotential system, calculated numerically. The dashed lines correspond to the theoretical c_e and c_r. The velocity c_r was calculated in the potential case (light dashed line) and in the nonpotential case (dark dashed line). The velocity c_e is the same in both cases. The light continuous line presents the velocity measured for the potential case (see Fig. 1), and the black continuous line presents the velocity in the nonpotential case. Here $a=b=-1.0$ and $\lambda=2$.

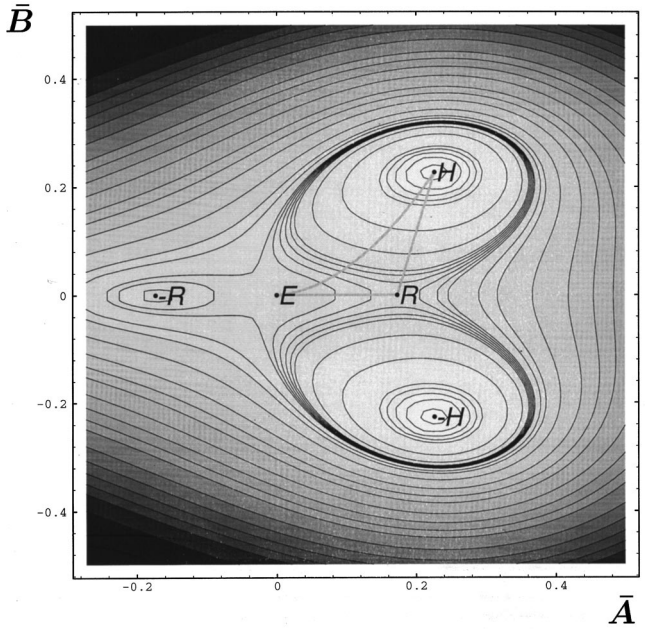

FIG. 4. Isolines of the potential $V(\bar{A},\bar{B})$ at γ in region $B(\gamma=0.03)$, $\lambda=2$. The horizontal axis is $\bar{A}$ and the vertical axis is $\bar{B}$. H and $-H$ are the hexagon stationary points, R and $-R$ are the roll stationary points, and E is the equilibrium stationary point.

III. ''STABLE-UNSTABLE'' FRONT

In this section we describe the behavior of the hexagon-equilibrium transition front in the region $\gamma>0$, where the hexagons are stable and the quiescent state (mechanical equilibrium) is unstable.

A. Potential case

1. Formulation of the problem

First, let us discuss the potential case ($\hat{B}=\hat{K}=0$) that was formerly studied in [17]. Here we present some additional results. Later on, we assume $\lambda>1$. We should take into account that at $\gamma>0$, in addition to Eqs. (8) and (9), there exist two stationary spatially uniform solutions of Eq. (7) that correspond to the roll pattern

$$A=\pm\sqrt{\gamma}, \quad B=0. \tag{43}$$

We will consider the region $0<\gamma<(\lambda-1)^{-2}$ where the hexagons are stable and the rolls and the quiescent state are unstable [1].

A front moving with the constant velocity c,

$$A(x,t)=\bar{A}(\xi), \quad B(x,t)=\bar{B}(\xi), \quad \xi=x-ct, \tag{44}$$

is governed by the system of equations (12) and (13). The map of the potential (15) in the case $\gamma>0$ is shown in Fig. 4.

The fronts correspond to trajectories leading from one extremum point to another. We can expect the existence of hexagon-equilibrium fronts (H-E), roll-equilibrium fronts (R-E), and hexagon-roll fronts (H-R).

2. Velocity calculations

In the case of a front propagating from a stable state (hexagons in our case) into an unstable (quiescent) state, the front velocity is known to be not unique [22]. However, it has been proved by Kolmogorov *et al.* [22], for the one-component nonlinear diffusion equation, that the system does prefer one velocity out of all possibilities (see also [23]). For a large class of multicomponent problems [which, however, does not include the system (7)] a similar result was established by Volpert *et al.* [24].

One can calculate the preferred velocity of propagation of any pattern into the unstable quiescent state by means of the linear marginal stability principle [25], which leads to the following relation:

$$c-\left.\frac{d\omega(k)}{dk}\right|_{k=k_*}=0, \tag{45}$$

where k_* satisfies

$$\mathrm{Im}[ck_*-\omega(k_*)]=0, \tag{46}$$

and $\omega(k)$ is the dispersion relation for the disturbances of the linearly unstable state. In the case of a front propagating into the equilibrium (quiescent) state,

$$\omega=i(\gamma-k^2); \tag{47}$$

hence one finds that

$$k_*=ic/2, \quad c=c_e\equiv 2\sqrt{\gamma}. \tag{48}$$

This velocity was found first by Kolmogoroff, Petrovsky, and Piscounoff (KPP) [22] for the case of a one-dimensional system with one stable and one unstable stationary points.

By the same method the velocity of propagation of the front into an unstable roll pattern is calculated [17]: linearizing Eqs. (7) around the roll solution $A=\sqrt{\gamma}$, $B=0$, one obtains

$$\frac{\partial\tilde{B}}{\partial t}=\gamma\tilde{B}+\frac{1}{4}\frac{\partial^2\tilde{B}}{\partial x^2}+\sqrt{\gamma}\tilde{B}-\lambda\gamma\tilde{B}. \tag{49}$$

Using the dispersion relation

$$\omega=i\left(\gamma-\frac{k^2}{4}+\sqrt{\gamma}-\lambda\gamma\right), \tag{50}$$

from Eq. (45), one finds $c=-ik_*/2$, and from Eq. (46),

$$c=c_r\equiv[\sqrt{\gamma}-(\lambda-1)\gamma]^{1/2}. \tag{51}$$

This speed exceeds c_e in the interval $0<(\lambda+3)^{-2}$.

In some cases, however, the ''generic'' front with the velocity calculated above is replaced by the ''nongeneric'' front [18,19] (see below).

3. Numerical results for the front dynamics

We solved the system (7) with boundary conditions

$$A=B=A_h \quad \text{at } x=0, \tag{52}$$

$$A=B=0 \quad \text{at } x=600,$$

for different γ's in the region of $0<\gamma<(\lambda-1)^{-2}\equiv\gamma_2$ where the hexagons are stable and the mechanical equilibrium state and rolls are unstable, and we measured the steady state velocity. We used two kinds of initial conditions: (1) $A=B=A_h$, $0\leqslant x\leqslant L/2$; $A=B=0$, $L/2<x\leqslant L$; and (2) $A=B=A_h$, $0\leqslant x<(L-L_i)/2$; $A=\sqrt{\gamma}$, $B=0$, $(L-L_i)/2<x<(L+L_i)/2$; $A=B=0$, $(L+L_i)/2<x\leqslant 600$. Different behavior of the fronts was observed in three main regions. In region A, $\gamma>0$ but close to zero, and the front is described by the nongeneric solution (see below). In region B, $\gamma>0$ and far from zero, and the KPP criterion may be used; thus the front moves with the velocity $c_e=2\sqrt{\gamma}$. In this region an intermediate layer of unstable rolls is observed. The lines of the rolls are parallel to the front. In the steady state, the roll layer has a constant finite width, thus forming two fronts, both moving with the same velocity. In region C, $\gamma>(3+\lambda)^{-2}$, which is the point where c_e becomes greater than c_r and each one of the fronts moves with its own velocity, thus forming an intermediate roll layer that grows in time. In Fig. 1 we can see all the results for the velocities of the fronts.

Let us discuss the behavior of the front in each region in more detail.

Region A: Nongeneric front. According to Eq. (48), the velocity $c_e=0$ as $\gamma=0$. However, in reality $c(\gamma)$ is continuous in the point $\gamma=0$. We will show that the system selects the nongeneric solution.

The asymptotic behavior of $\overline{A}$, $\overline{B}$ governed by Eqs. (12) and (13), is

$$\overline{A}\sim e^{\kappa_A\xi}, \quad \overline{B}\sim e^{\kappa_B\xi} \text{ as } x\to\infty, \tag{53}$$

where

$$\kappa_A^{\pm}=-\frac{c}{2}\pm\tfrac{1}{2}\sqrt{c^2-4\gamma},$$
$$\kappa_B^{\pm}=-2c\pm 2\sqrt{c^2-\gamma}. \tag{54}$$

For $\gamma<0$, we have $\kappa_A^-<0$ and $\kappa_A^+>0$; thus the asymptotics of the front tail for A is definitely determined by $\kappa_A=\kappa_A^-$. When γ changes sign from negative to positive, both κ_A's become negative. Because $|\kappa_A^+|<|\kappa_A^-|$, typically the solution tending to zero behaves like $\sim\exp(\kappa_A^+x)$ as $x\to\infty$, but there exists also a special trajectory with the asymptotics $\sim\exp(\kappa_A^-x)$. In our simulation, we measured $\kappa_A(\gamma)$ in the tail of the function A at large x, and we found that the measured κ_A agrees with the *nongeneric* value κ_A^- calculated according to Eq. (54), with c taken from the simulation. The results are shown in Fig. 5. Thus we see that the system prefers the nongeneric solution, with $\kappa_A=\kappa_A^-$.

Region B: Roll strip between the synchronized R-E and H-R fronts. For larger values of γ, the simulations show that the system selects a ''generic'' solution with the velocity $c_e=2\sqrt{\gamma}$.

Before starting to discuss the results of numerical simulations, let us consider the set of front solutions. A front moving with a prescribed velocity c is governed by the system (12) and (13), which has a certain ''mechanical'' interpretation: a ''particle'' (with anisotropic mass and friction) moves in the potential $V(\overline{A},\overline{B})$ from H to E. Because the point E, which corresponds to a minimum of the potential, is stable in the framework of the system (12) and (13), it has a finite (four-dimensional) basin of attraction, while the point H has a two-dimensional unstable manifold (see below). The intersection of the latter manifold with the attraction basin of E is two dimensional; thus the front between the hexagonal pattern H and the equilibrium (quiescent) state E is not unique, even for the selected value of $c=\gamma\sqrt{2}$. Let us emphasize that the ''stability'' of a fixed point of the system (12) and (13) in the sense of the ''evolution'' in ξ does not coincide with the stability of the corresponding solution of Eq. (7) in the usual sense.

We solved the system (12) and (13) in order to find possible front solutions. Linearizing Eqs. (12) and (13) in the vicinity of a hexagon solution $\overline{A}=\overline{B}=A_h$, and taking $\overline{A}=A_h+\tilde{A}$, $\overline{B}=A_h+\tilde{B}$, where $\tilde{A}$ and $\tilde{B}$ are small perturbations around the hexagon solution, we obtain

$$\tilde{A}_{\xi\xi}+c\tilde{A}_{\xi}+(\gamma-3A_h^2-2\lambda A_h^2)\tilde{A}+(2A_h-4\lambda A_h^2)\tilde{B}=0, \tag{55}$$

$$\tfrac{1}{4}\tilde{B}_{\xi\xi}+c\tilde{B}_{\xi}+(A_h-2\lambda A_h^2)\tilde{A}+[\gamma+A_h-(3+4\lambda)A_h^2]\tilde{B}=0. \tag{56}$$

Substituting $(\tilde{A},\tilde{B})=(\hat{A},\hat{B})e^{\mu\xi}$, we obtain the characteristic polynomial for the eigenvalues μ:

$$[\mu^2+c\mu+\gamma-(3+2\lambda)A_h^2][\tfrac{1}{4}\mu^2+c\mu+\gamma+A_h-(3+4\lambda)A_h^2]-(2-4\lambda A_h)(1-2\lambda A_h)A_h^2=0. \tag{57}$$

Calculating μ numerically by MATHEMATICA software, we found two positive and two negative eigenvalues for each γ in region B; hence the fixed point corresponding to the hexagons indeed has a two-dimensional unstable manifold. Also, we found the eigenvectors $\vec{u}^{(1)},\vec{u}^{(2)}$ for the positive eigenvalues.

Defining

$$y_1=\overline{A},$$
$$y_2=\overline{A}',$$
$$y_3=\overline{B},$$
$$y_4=\overline{B}', \tag{58}$$

we rewrote Eqs. (12) and (13) in the form

$$y_1'=y_2,$$
$$y_2'=-cy_2-\gamma y_1-y_3^2+y_1^3+2\lambda y_1y_3^2,$$
$$y_3'=y_4,$$
$$y_4'=-4cy_4-4\gamma y_3-4y_1y_3+4\lambda y_3y_1^2+4(1+\lambda)y_3^3, \tag{59}$$

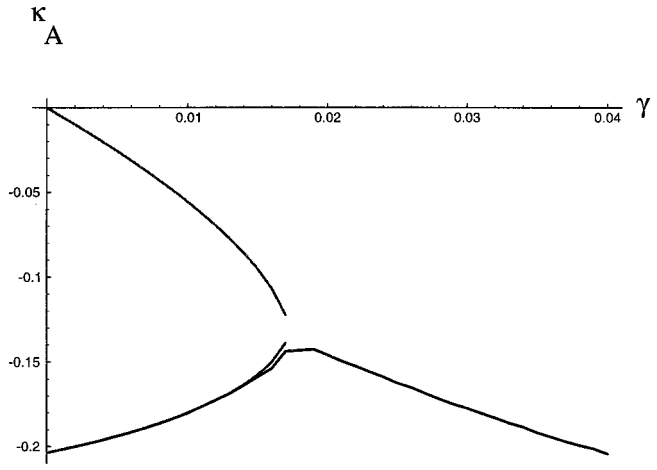

FIG. 5. Generic and nongeneric curves κ_A vs γ calculated for the value of c obtained numerically. The light lines are generic κ_A^+ (upper) and nongeneric κ_A^- (lower). The dark line is κ_A measured from the numerical results. We see that close to $\gamma=0$ our system prefers the nongeneric κ_A^-.

and solved the system (59) numerically with the initial conditions

$$\vec{y}(0)=\begin{pmatrix} A_h \\ 0 \\ A_h \\ 0 \end{pmatrix} + \epsilon\vec{u}^{(1)}\cos\theta + \epsilon\vec{u}^{(2)}\sin\theta, \quad \epsilon \ll 1 \quad (60)$$

(as if we were pushing the particle from the top point H in Fig. 4 in the direction characterized by the angle θ).

Indeed, we found a rather narrow interval of angles (the width of this interval is dependent on the ϵ we choose) near $\theta=-\pi/2$, which leads to a hexagon-equilibrium front. All other angles caused a divergent solution that went from $A=B=A_h$ up to infinity. As we assumed, there was no uniqueness of the front solution; even for the fixed value of $c=c_e$, there exists a family of solutions characterized by different widths L_r of the intermediate roll belt. Later on we define the width of the roll belt L_r as the distance between

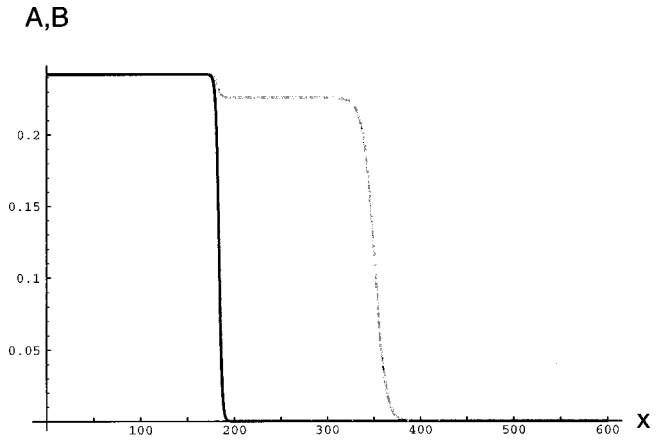

FIG. 6. The shapes of the envelope functions in region C, after the hexagon-roll front is separated from the roll-equilibrium front and both fronts move with different velocities. The light line corresponds to the amplitude A and the dark line corresponds to the amplitude B. On the left, where $A=B\approx A_h$, there are the hexagons; on the right, where $A,B\to 0$, there is the equilibrium, and in the middle, where $A\approx A_r$ and $B\to 0$, there is the intermediate layer of rolls parallel to the front.

the point where A reaches $A_h/2$ and the point where B reaches $A_h/2$. If we increase the angle θ monotonically, for the lowest values of θ no intermediate roll layer is observed. As θ grows, the width of the roll layer grows as well, and for a certain value of θ it tends to infinity. It should be noted that $B(\xi)$ is positive everywhere only if L_r is less than a certain value $L_*(\gamma)$. If $L_r>L_*(\gamma)$, we observe oscillations in B around $B=0$, i.e., B is not positive anymore.

Let us discuss now the results of direct simulations of the system (7) performed by means of a finite-difference method. As the initial conditions, we took some functions $A(x,0)\geqslant 0$, $B(x,0)\geqslant 0$ that described a hexagon-equilibrium front, with a certain intermediate roll layer of the width $L_i \geqslant 0$. At large t we obtained a steady front between the hexagons and the equilibrium with an intermediate layer of rolls (see Fig. 6). The intermediate layer of rolls becomes wider as γ grows. Obviously, $B(x,t)$ is non-negative for any t for the initial conditions used; thus we can never get steady oscillat-

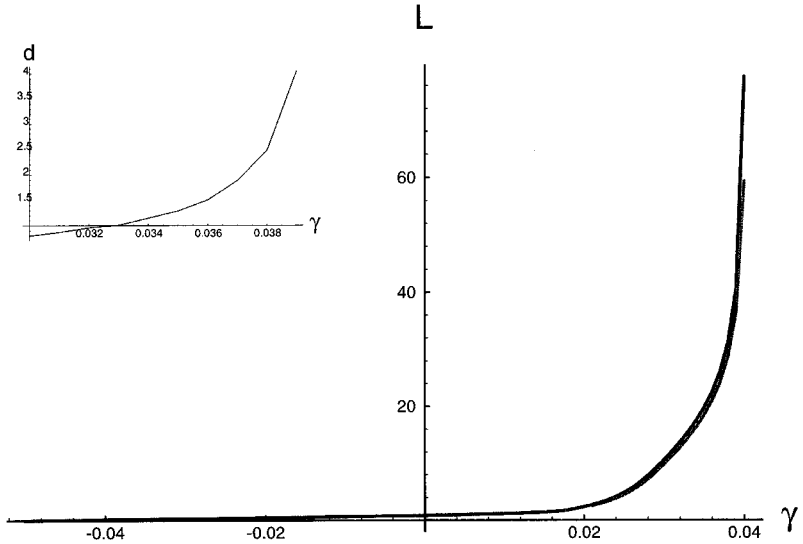

FIG. 7. The width of the intermediate roll layer that develops between the stable hexagonal pattern and unstable equilibrium. The dark line is L_f, the finite roll layer width. The light line is L_*, the maximum length of the roll layer that is possible with $B\geqslant 0$, obtained in the ''mechanical'' simulations [system (59)]. The small inset shows the difference between the two lengths $d=L_*-L_f$ in the region $0.03\leqslant\gamma<0.04$.

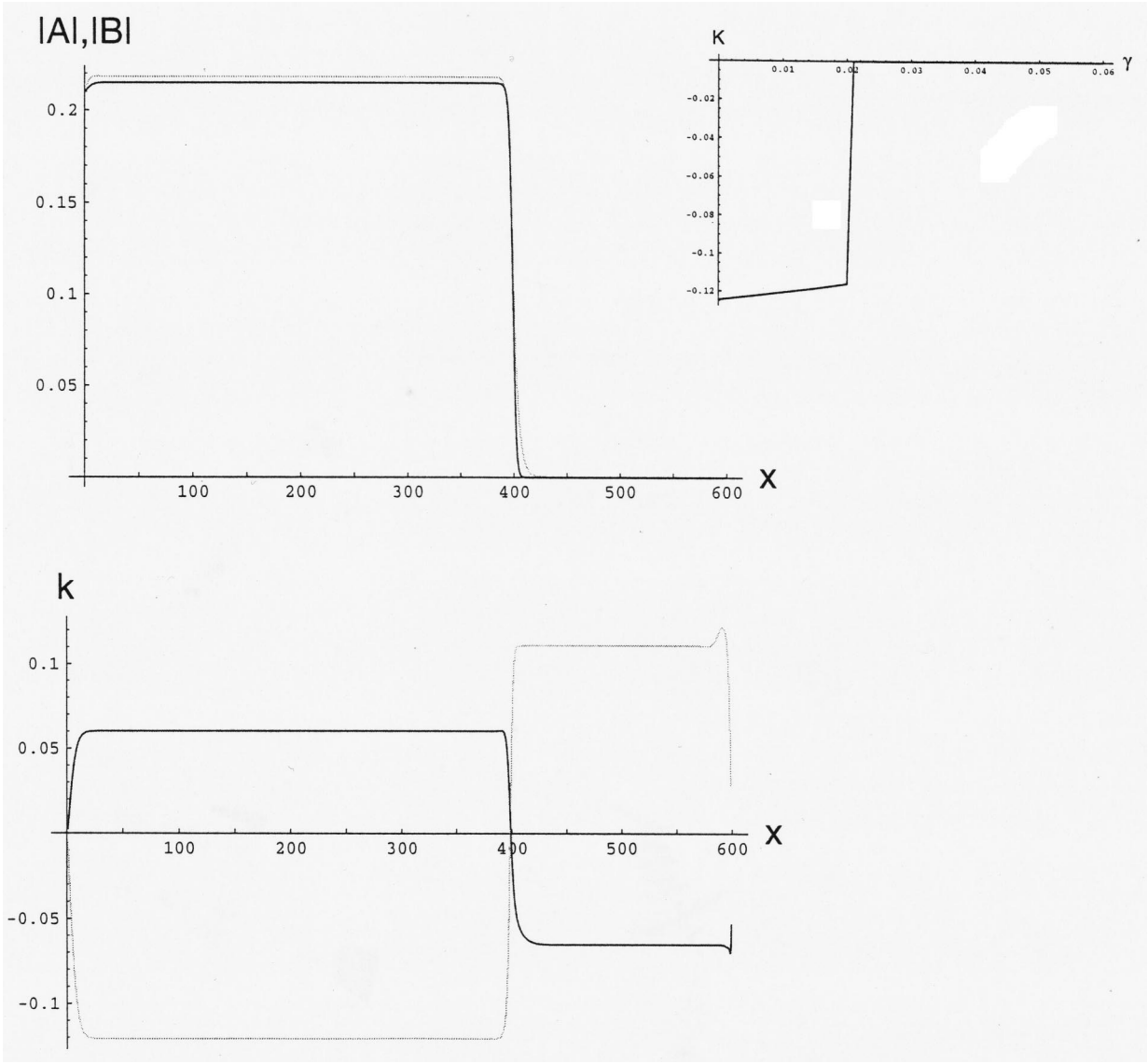

FIG. 8. The envelope shape for the nonpotential system $a=b=-1.0$ and γ in region $A(\gamma=0.010)$, k being the phase gradient $\partial\Phi/\partial x$. We see a constant phase gradient throughout the area of the hexagons, another constant phase gradient in the equilibrium area, and a large change of the phase gradient at the front. The light lines are the absolute value and phase gradient of the function *A*, and the dark lines are those of the function *B*. The small inset shows the phase gradient of *A* vs γ. In the range of $0\leqslant\gamma\leqslant 0.02$ the phase gradient changes linearly with γ, and for higher γ's the phase gradient vanishes. In between there is a peculiarity discussed in the text.

ing solutions with $L_r > L_*(\gamma)$, as $t\to\infty$. Unexpectedly, we found that the finite width of the roll strip L_f was *independent* of the initial value L_i, despite the nonuniqueness of the front solutions discussed above. We observed that the roll strip became wider as γ grew.

We conjecture that the system prefers the largest width of the roll intermediate layer that is permitted by the condition that *B* does not change sign, i.e., the width of the intermediate layer, selected by our system, is $L_f(\gamma)=L_*(\gamma)$.

In Fig. 7 one can see the comparison between L_f, the finite roll layer width, and L_*, the width where the oscillations start. There is a very good coincidence between the two quantities.

Region C: Front splitting. In the region *B* discussed above, as γ grows, the width of the intermediate region of rolls grows but is finite. This is true as long as $c_e < c_r$. As γ reaches the point where $c_e=c_r$, i.e., $\gamma=(\lambda+3)^{-2}$, this behavior changes. When $c_e > c_r$, the H-R front stars lagging behind the R-E front and they separate, each of them moving at its own velocity. Thus the width of the intermediate layer becomes infinite in the long run, and there is no steady state solution. The velocities we obtained numerically for c_e and c_r are exactly those defined by Eqs. (48) and (51). The results are shown in Fig. 1, at the far right of the graph.

The solution itself looks as in Fig. 6. Both fronts move to the right while the R-E front moves faster than the H-R front, thus widening the roll layer more and more.

We studied also the ''mechanical'' system Eq. (59) in region *C* with $c=c_e$, and found a variety of front solutions with arbitrary widths L_r of the roll belt, up to infinity. No oscillations of *B* occurred in this region at any values of the width L_r. Thus, in the region *C*, as in the region *B*, there exists a family of front solutions that describe a synchronized motion of the R-E and H-R fronts with a finite distance be-

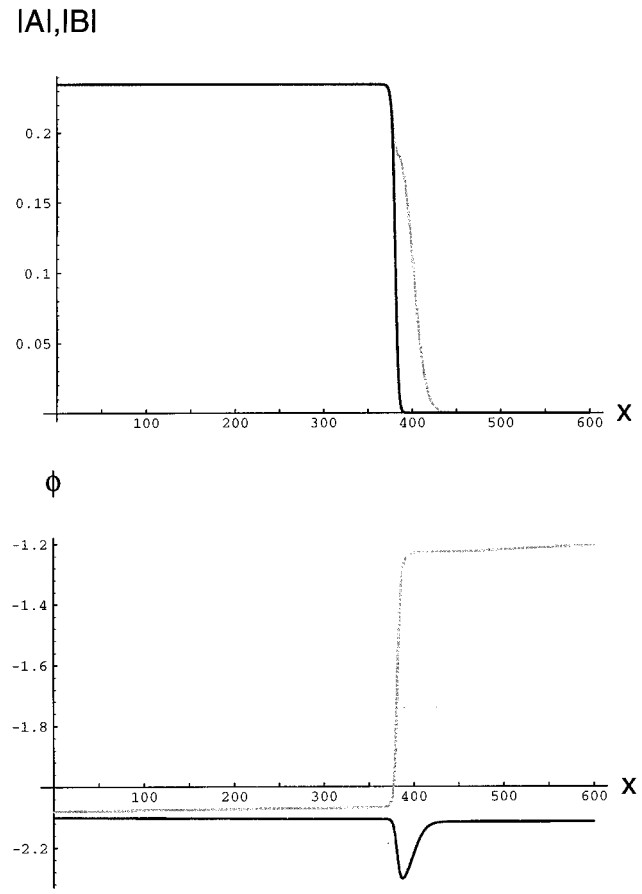

FIG. 9. The envelope shape for the nonpotential system $a=b=-1.0$ and γ in region $B(\gamma=0.041)$. The beginning of a small intermediate roll layer can be seen here. The phase is constant far from the front and exhibits a large change at the front. The light lines are the absolute value and phase of the function A, and the dark lines are those of the function B.

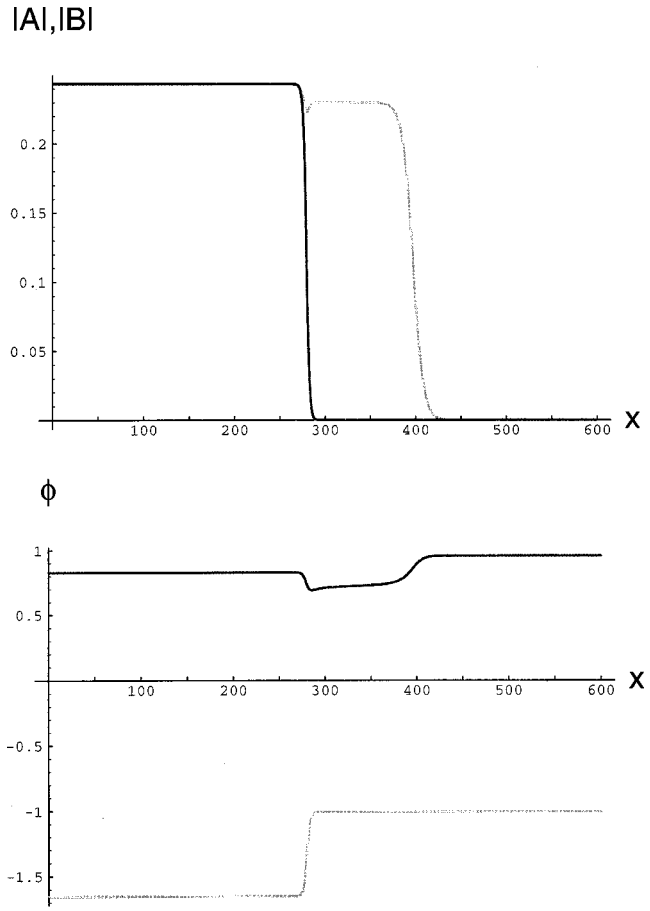

FIG. 10. The envelope shapes for the nonpotential system $a=b=-1.0$ and γ in region $C(\gamma=0.053)$. We can see hexagons on the left and equilibrium on the right and rolls in the intermediate layer. The phase is constant far from the front and has a large change at the front. The phase inside the roll layer is close to constant as well. The light lines are the absolute value and phase of the function A, and the dark lines are those of the function B.

tween them. However, as the direct simulation of Eqs. (7) shows, the system prefers the widest L_f possible, which is infinity in this case.

Noise influence in region C. We would like to emphasize that because the roll pattern strip is unstable, the phenomenon of the front splitting is sensitive to noise. Indeed, the disturbance of the variable B generated by noise on the R-E front is amplified in the region of rolls and eventually generates a hexagonal pattern at a certain distance L_f from the R-E front which is determined by the spatial growth rate $|\kappa_B^r|$ of the disturbance and its initial amplitude ϵ: $\epsilon \exp(|\kappa_B^r|L_f)\sim 1$, therefore

$$|\kappa_B^r|L_f \sim \ln\frac{1}{\epsilon}. \tag{61}$$

Thus, one will observe a noise-generated synchronized motion of the R-E and H-R fronts (similar to that predicted in region B for a deterministic system) even in the region C.

Because of the existence of a *numerical inaccuracy*, one can expect that this phenomenon will also be observed in numerical simulations of a deterministic system. Indeed, when using a less precise numerical scheme (based on the finite elements method), we observed that in the transition from region B to region C the roll layer width L_f grew but remained finite. Both fronts R-E and H-R moved with the common velocity $c_e=2\sqrt{\gamma}$.

To justify our conjecture that the ''synchronization'' of the motions of the R-E and H-R fronts in region C was caused by the spatial amplification of a numerical inaccuracy generated on the R-E front, we calculated in that region the quantity $|\kappa_B^r|(\gamma)L_f(\gamma)$. Recall that $|\kappa_B^r|$ is the spatial growth rate of a small B disturbance in the background of the roll pattern $A=\sqrt{\gamma}$, $B=0$ [i.e., $B\sim\exp(-|\kappa_B^r|x)$; the validity of the latter relation in the region of rolls was checked numerically]. We found that the quantity $|\kappa_B^r(\gamma)|L_f(\gamma)$ was *constant* for any values of γ in region C, in agreement with the formula (61), while in region B this quantity was smaller and increased monotonically with growing γ.

The phenomenon described of the front motion synchronization was a result of an inaccuracy of the numerical method, and was eliminated by its improvement (i.e., in the principal simulations described above, the distance between fronts reached the size of the simulation region L). Note, however, that systems with noise are much more realistic in the real world.

Also, let us note that Eq. (61) provides a quantitative de-

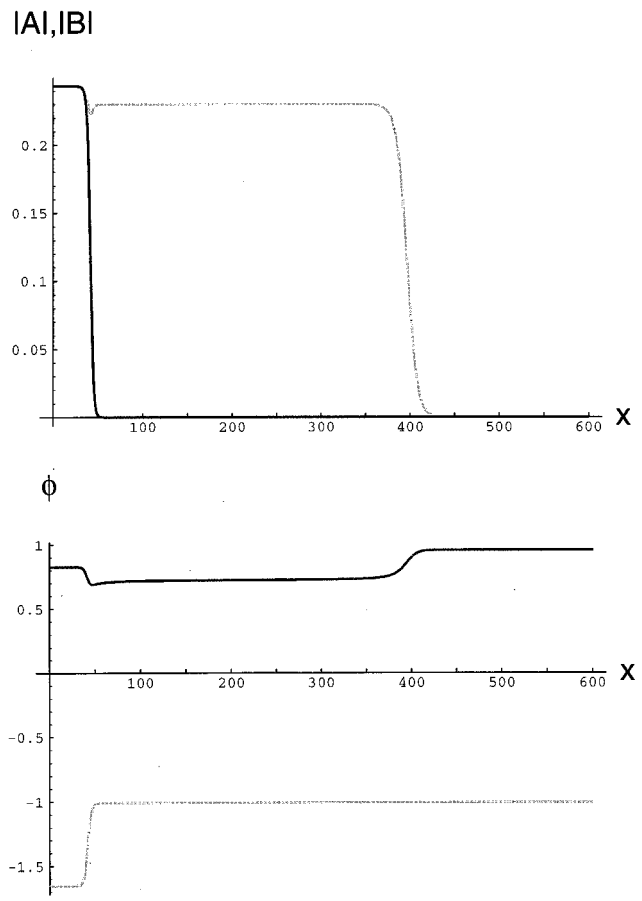

FIG. 11. The envelope shapes for the nonpotential system $a=b=-1.0$ and γ in region $C(\gamma=0.053)$. This is the same simulation as in Fig. 10 but after some time has passed. We see that the intermediate roll layer is much larger now. The phase is constant far from the front and has a large change at the front. The phase inside the rolls is constant as well. The light lines are the absolute value and phase of the function A, and the dark lines are those of the function B.

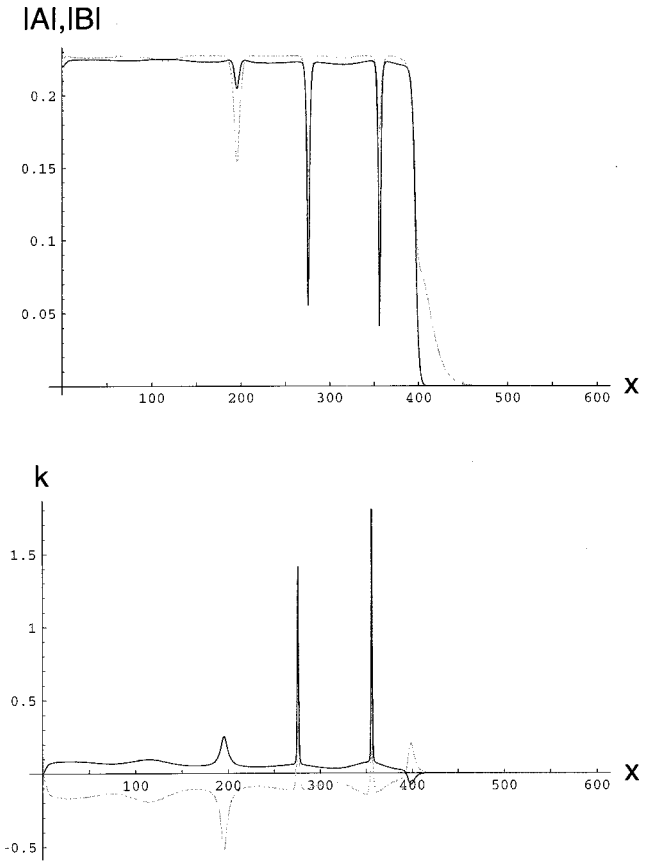

FIG. 12. The envelope shapes for the nonpotential system $a=b=-1.0$ and $\gamma=0.020$, k being the phase gradient $\partial\Phi/\partial x$. For this value of γ the hexagons are suspected to be unstable for a high value of the phase gradient. The phase gradient is relatively high for both amplitude functions and the hexagon amplitude absolute value is penetrated by sharp cuts at the points where the phase gradient is particularly high. As time increases, this shape moves to the right and does not change.

scription of the mechanism of the front motion synchronization due to the intrinsic instability of the roll pattern suggested in [20].

B. Nonpotential case

1. Velocity calculations

We calculated the velocities of the front propagation by means of the marginal stability criterion.

Hexagon/roll-equilibrium front. Linearizing Eq. (40) in the vicinity of the equilibrium solution $A=0$, $B=0$, we obtain the same velocity as in the potential case, because all the nonpotential terms disappear in the linearization. Thus

$$c_e=2\sqrt{\gamma}. \tag{62}$$

Hexagon-roll front. We linearize Eq. (41) in the vicinity of the roll solution,

$$A=\sqrt{\gamma}+\tilde{A},\qquad B=0+\tilde{B}, \tag{63}$$

where $\tilde{A}$ and $\tilde{B}$ are small perturbations of the roll solution, and obtain

$$\frac{\partial\tilde{B}}{\partial t}=\gamma(1-\lambda)\tilde{B}+\frac{1}{4}\frac{\partial^2\tilde{B}}{\partial x^2}+\sqrt{\gamma}\tilde{B}^*+i\left(a-\frac{b}{2}\right)\sqrt{\gamma}\frac{\partial B^*}{\partial x}. \tag{64}$$

Then we separate the equation into its real and imaginary parts:

$$\frac{\partial\tilde{B}_r}{\partial t}=[\gamma(1-\lambda)+\sqrt{\gamma}]\tilde{B}_r+\frac{1}{4}\frac{\partial^2\tilde{B}_r}{\partial x^2}+\left(a-\frac{b}{2}\right)\sqrt{\gamma}\frac{\partial\tilde{B}_i}{\partial x}, \tag{65}$$

$$\frac{\partial\tilde{B}_i}{\partial t}=[\gamma(1-\lambda)-\sqrt{\gamma}]\tilde{B}_i+\frac{1}{4}\frac{\partial^2\tilde{B}_i}{\partial x^2}+\left(a-\frac{b}{2}\right)\sqrt{\gamma}\frac{\partial\tilde{B}_r}{\partial x}, \tag{66}$$

substitute

$$\tilde{B}_{r,i}=\int \exp\{i[kx-\omega(k)t]\}\tilde{B}_{r,i}(k)dk, \tag{67}$$

and obtain the dispersion relation

$$\omega = i\left(-\frac{k^2}{4} + \gamma(1-\lambda) \mp \sqrt{[1-k^2(a-b/2)^2]\gamma} \right). \quad (68)$$

As in the potential case, we obtain an expression for the velocity c_r,

$$c_r = \frac{d\omega}{dk} = -i\frac{k}{2} \pm i\sqrt{\gamma}\frac{k(a-b/2)^2}{\sqrt{1-(a-b/2)^2k^2}}, \quad (69)$$

and from the relation

$$\mathrm{Im}[ck-\omega(k)]=0$$

we find

$$\left(\frac{k^2}{4}+\gamma(1-\lambda)\right)\sqrt{1-k^2(a-b/2)^2} = \pm\sqrt{\gamma}, \quad (70)$$

where the $\pm$ sign is with respect to the $\pm$ sign in Eq. (69).

Solving Eq. (70) by MATHEMATICA software, we obtain real k solutions for the equation with $+\sqrt{\gamma}$, and pure imaginary k solutions for the equation with $-\sqrt{\gamma}$. As we expect real values for c, it is clear from Eq. (69) that only the imaginary k's are the proper ones, and they should be substituted into Eq. (69) with the minus sign in the last term.

We calculated c_r for a whole range of $\gamma \geqslant 0$, and the results are shown in Fig. 3.

2. Numerical results

We solved the system (40) and (41) numerically, with $a=b=-1.0$, as in the case of the stable-stable front. The results for the front velocity are shown in Fig. 3, and those for the phase gradient are shown in the inset to Fig. 8. Note that our results are rather similar to those of [20]. As in the potential case, there are three characteristic regions.

In region A the system selects the ''nongeneric'' solution, so that the velocity is continuous when crossing the value $\gamma=0$. We measured κ_A at the tail of signal A and obtained a value that is very close to the calculated κ_A^- from Eq. (54) that we obtained previously in the potential case (recall that the nonpotential terms disappear by linearization).

In region A, the phase gradient $K=d\phi/dx$ changes linearly with γ, as can be seen in the inset to Fig. 8. A typical envelope form in this region can be seen in Fig. 8.

In region B the front moves with velocity c_e. In this case, as in the potential system, we observe an intermediate roll layer between the hexagons and equilibrium. Both fronts, H-R and R-E, move with the same velocity in the steady state, and thus the width of the roll layer is constant. The envelope shape, including absolute value and phase for one of the γ's in this region, can be seen in Fig. 9.

The phase in this case becomes constant after a long time, apart from the front area, where it exhibits a large change.

In region C the two fronts separate and move with different velocities, c_e determined by the KPP criterion (62) and c_r given by Eq. (69). In Figs. 10 and 11 we can see the envelope shapes obtained from the numerical calculations on the nonpotential system with $a=b=-1.0$ and γ in region C. One can see that the roll layer becomes wider with time, and the phase in the roll layer settles to a constant value.

In the transition region between regions A and B one can observe some rather unusual shapes of the front (see Fig. 12). The phase gradient is very steep for both amplitude functions near some three points inside the hexagon layer, and at these points the absolute values of amplitudes have sharp minima. As time increases, this structure moves to the right as the whole and does not change its shape. We solved the same problem with other numerical time and space steps, such that with the new steps the value of $\Delta x^2/\Delta t$ became larger, giving a better stability. We obtained the same results, and therefore we conclude that this phenomenon is not due to numerical instability. Probably in the case shown in Fig. 12 the phase gradient is so high that the hexagon wave number selected by the front turns out to be outside the stability region.

IV. CONCLUSIONS

We found that nonpotential effects may greatly influence the dynamics of fronts between convecting patterns. First, they determine the wave numbers of the selected pattern, which in some cases may lead to the selection of an unstable pattern. Also, they influence the selected velocities of simple fronts and shift the splitting point of the hexagon-equilibrium front. In the case of a compound front between hexagons and the quiescent state, an additional selection criterion defining the width of the roll pattern belt is suggested. The physical nature of this selection should be the subject of a special investigation.

ACKNOWLEDGMENT

The authors are indebted to B. A. Malomed for valuable discussions.

[1] F. H. Busse, J. Fluid Mech. **30**, 625 (1967).
[2] A. Gailitis, J. Fluid Mech. **82**, 401 (1977).
[3] M. Silber and E. Knobloch, Physica D **30**, 83 (1988).
[4] A. Golovin, A. A. Nepomnyashchy, and L. M. Pismen, Physica D **81**, 117 (1995).
[5] Y. Pomeau, Physica D **23**, 3 (1986).
[6] A. C. Newell and J. A. Whitehead, J. Fluid Mech. **38**, 279 (1969).
[7] L. A. Segel, J. Fluid Mech. **38**, 203 (1969).
[8] B. A. Malomed, A. A. Nepomnyashchy, and M. I. Tribelsky, Phys. Rev. A **42**, 7244 (1990).
[9] A. Hari and A. A. Nepomnyashchy, Phys. Rev. E **50**, 1661 (1994).
[10] H. R. Brand, Prog. Theor. Phys. Suppl. **99**, 442 (1989).
[11] G. H. Gunaratne, Q. Ouyang, and H. Swinney, Phys. Rev. E **50**, 2802 (1994).
[12] J. R. M. Pontes, Ph.D. Thesis, Université Libre de Bruxelles, 1994 (unpublished).
[13] E. A. Kuznetsov, A. A. Nepomnyashchy, and L. M. Pismen, Phys. Lett. A **205**, 261 (1995).

[14] A. Golovin, A. A. Nepomnyashchy, and L. M. Pismen, J. Fluid Mech. **341**, 317 (1997).
[15] J. Bragard and M. G. Velarde, J. Fluid Mech. **368**, 165 (1998).
[16] E. A. Kuznetsov and M. D. Spector, J. Appl. Mech. Tech. Phys. **21**, 220 (1980).
[17] L. M. Pismen and A. A. Nepomnyashchy, Europhys. Lett. **27**, 433 (1994).
[18] W. van Saarlos, Phys. Rev. A **39**, 6367 (1989).
[19] J. A. Powell, A. C. Newell, and C. K. R. T. Jones, Phys. Rev. A **44**, 3636 (1991).
[20] Z. Csahók and C. Misbah, Europhys. Lett. **47**, 331 (1999).
[21] B. A. Malomed, A. A. Nepomnyashchy, and A. E. Nuz, Physica D **70**, 357 (1994).
[22] A. Kolmogorov, I. Petrovsky, and N. Piscounoff, Bull. Univ. État Moscow Ser. Int. A **1**, 105 (1937) [reprinted in *Dynamics of Curved Fronts*, edited by P. Pelcé (Academic, San Diego, 1988)].
[23] D. G. Aronson and H. F. Weinberger, Adv. Math. **30**, 33 (1978).
[24] A. I. Volpert, V. A. Volpert, and V. A. Volpert, Am. Math. Soc. Trans. **140** (1), (1994).
[25] G. T. Dee and W. van Saarloos, Phys. Rev. Lett. **60**, 2641 (1988).